Research article

Experimental spectral characterization, Hirshfeld surface analysis, DFT/TD-DFT calculations and docking studies of (2Z,5Z)-5-(4-nitrobenzylidene)-3-N(2-methoxyphenyl)-2-N'(2-methoxyphenylimino) thiazolidin-4-one

Ahmed Djafri [a,b], Fouzia Perveen [c], Nadia Benhalima [b,d], Nawel Khelloul [b,e], Rachida Rahmani [b,f], Ayada Djafri [g], Abdelkader Chouaih [b], Mohammed Benali Kanoun [h], Souraya Goumri-Said [i,*]

[a] Centre de Recherche Scientifique et Technique en Analyses Physico-chimiques (CRAPC), BP 384-Bou-Ismail-RP, 42004, Tipaza, Algeria
[b] Laboratory of Technology and Solid Properties (LTPS), Abdelhamid IbnBadis University, BP 227, Mostaganem, 27000, Algeria
[c] Research Center for Modeling and Simulations (RCMS), National University of Sciences and Technology, H-12 Campus, Islamabad, Pakistan
[d] Département de physique, Faculté des sciences, Université Dr. Moulay Tahar, BP138, EN-NASR, 20000, Saida, Algeria
[e] Faculty of Sciences and Technology, Mustapha Stambouli University of Mascara, B.P.763, 29000, Mascara, Algeria
[f] Département de Génie des procédés, Centre Universitaire de Relizane, Algeria
[g] Laboratoire de Synthèse Organique Appliquées, Faculté des Sciences Exactes et Appliquées, Département de Chimie, Université Oran-1, Algeria
[h] Department of Physics, College of Science, King Faisal University, P.O. Box 400, Al-Ahsa, 31982, Saudi Arabia
[i] College of Science, Physics Department, Alfaisal University, P.O. Box 50927, Riyadh, 11533, Saudi Arabia

ARTICLE INFO

ABSTRACT

We reported an experimental and theoretical spectroscopic studies of (2Z,5Z)-5-(4-nitrobenzylidene)-3-N (2-methoxyphenyl)-2-N' (2-methoxyphenylimino) thiazolidin-4-one ($C_{24}H_{19}N_3O_5S$) molecule, using FT-IR, NMR spectroscopy, and density functional theory (DFT) via time-dependent schema (TD-DFT) respectively. The molecular inter-contacts were explored using Hirshfeld surfaces (HS) analysis method. Vibrational frequencies, gauge-independent atomic orbital (GIAO)^{1}H and^{13}C NMR chemical shift values and frontier molecular orbitals (FMOs) have been calculated from the optimized structure of the molecule by DFT/B3LYP functional with 6-31G(d, p) basis set. Our theoretical results show a good agreement with the experimental data. The calculated UV-visible spectrum employing TD-DFT shows electronic transitions at 388 nm and 495 nm. To get insight on the charge interaction happening inside the molecule, HOMO and LUMO were scrutinized and their calculated energy gap was found to be 2.96 eV. The molecular docking was analyzed via interplay study ofacetyl cholinesterase, and Butyrylcholinesterase using molecular docking methodology.

1. Introduction

In the last few decades, the design, elaboration and synthesis of new molecules became an active area of research by reason of their widespread applications in several emerging fields such as molecular electronics [1] and nano-biotechnology [2]. In particular, organic molecules and conductive polymers have been already used in many electronic devices such as organic solar cells [3, 4] and single-molecule transistors [5, 6] to name only two. An important class of molecules are the thiazole derivatives. The latter are organic compounds that have five-membered molecular ring structures. They have been emerged as promising materials for several applications in organic electronics and chemical industries including food and pharmaceuticals. As a biologically active

agent, thiazole has attracted many research in biology [7, 8, 9, 10]. It has been displayed that the thiazole moiety has antimicrobial activity [11, 12] and the thiazole ring and its compounds are very important pharmacophore [13] and they showed anti-convulsing, anti-inflammatory and anti-tumoralactivity [14].

In a recent work, we have determined the structure of the (2Z,5Z)-5-(4-nitrobenzylidene)-3-N(2-methoxyphenyl)-2-N'(2methoxyphenylimino) thiazolidin-4-one molecule both experimentally using spectroscopic FT-IR, (^{1}H,^{13}C) NMR, X-ray single crystal diffraction (XRD) and technically usingB3LYP/6-31G(d, p) [15]. The structure and composition of our molecule are shown in Figure 1. We aim in this paper, to further extend our analysis by studying the vibrational properties and chemical shifts of the $C_{24}H_{19}N_3O_5S$ molecule, experimentally applying

* Corresponding author.
  E-mail address: sosaid@alfaisal.edu (S. Goumri-Said).

UV-Visible, NMR spectroscopy and theoretically using Natural Bond Orbital (NBO) and Frontier Molecular Orbitals (FMOs) calculations within the DFT at the B3LYP/6-31G(d, p) level. On the microscopic scale, the later provide a powerful tool to investigate the electronic, magnetic and optical properties of atoms, molecules and condensed phases [16] and their outcomes are proved to fit very well with experiments [17]. It is helpful to conduct a comparison between experimental and theoretical spectra to determine proper assignments and understand the origin of the chemical shift in molecular structure. In order to predict theoretically the UV-Vis spectra of the present molecular system, we have employed a time-dependent (TD-DFT) known to one of the most accurate approaches as regard for computational cost and findings efficiency [18, 19]. For the ^{1}H and ^{13}C chemical shifts, we have used Gauge independent atomic orbital theory (GIAO) [20, 21]. The evaluated HOMO and LUMO energies confirm the existence of charge transfer occurring in the molecule. Throughout the paper, we compared the experimental data with the calculated results.

2. Experimental and theoretical methodologies

FT-IR spectrum was recorded in the 4000–400 cm^{-1} region with a JASCO 4200 FT-IR spectrometer using KBr pellet. ^{1}H and ^{13}C-NMR spectra were recorded at 300 MHz, in CDCl$_3$, on a BRUKER Ac DPX-200 spectrometer. The chemical shifts are reported per million (ppm) down field from internal tetramethylsilane (TMS) (chemical shift in d values). Electronic absorption spectrum was measured on a Unicam UV–Vis spectrophotometer in chloroform solvent. Spectrums were recorded at room temperature. All calculations were performed with the Gaussian 03 software package [22] and Gauss-View program [23]. B3LYP method is employed to optimize the molecular structure [24, 25] of the C$_{24}$H$_{19}$N$_3$O$_5$S molecule leading to energy minima in the ground state using the 6-31G(d, p) basis set [26, 27].

3. Results and discussion

3.1. Optimized geometry

The geometrical parameters, namely bond lengths, bond angles, and dihedral angles for C$_{24}$H$_{19}$N$_3$O$_5$S molecule computed by DFT/B3LYP functional with 6-31G(d, p) basis set are listed together with the X-ray diffraction data [15]. The calculated and experimental geometrical parameters of the title compound were found to be close, which indicate that our calculations are good. The small differences can be due to the fact that the calculated values are collected in the gas phase, while experimental data are achieved in the solid state. To make a better comparison of the geometrical parameters, correlation graphs between the calculated and the experimental parameters of bond lengths, bond angles and dihedral angles are plotted and shown in Figure 2. The correlation values R^2 obtained by B3LYP functional with 6-31G(d,p) basis set are 0.994, 0.912, and 0.999 for bond lengths, bond angles and

dihedral angles, respectively. These graphs confirmed the good agreement between calculated and experimental results.

3.2. Hirshfeld surface analysis

Hirshfeld surface analysis is employed to estimate the distribution of close contact interactions [28]. The structure input file in cif format and the Crystal Explorer have been used to calculate respectively the Hirshfeld surfaces and the related 2D-Fingerprint plots [29]. In the d$_{norm}$ surface, any intermolecular interactions appear as a red spot as shown in Figure 3(a). The presences of π–π stacking interactions are indicated by red and blue triangles on the shape-index surface presented in Figure 3(b). As seen in Figure 3(c), the deep red color indicates hydrogen bonding contacts. For example, a deep red spot indicates the presence of a hydrogen bond, type C–H···O (between H7 and O3) and C–H···N (between H21 and N3). The 2-D fingerprint plots, which analysis all intermolecular contacts altogether and revealed that the principal intermolecular interactions s is of type H···H, H···O, H···C, H···N and C···C as shown in Figure 4(a). The two-dimensional fingerprint presentation shows that the majority of contacts are due to H···H interaction. This interaction constitute up to 35.8% of the Hirshfeld surface of the (2Z,5Z)-5-(4-nitro-

benzylidene)-3-N(2methoxyphenyl)-2-N'(2-methoxyphenylimino) thiazolidin-4-one molecule. For the present compound, H···O contacts that were attributed to C–H···OH–bond interactions, appear as two sharp symmetric spikes in the two-dimensional fingerprint map. The existence of these long spikes (displayed in Figure 4(d)) is a proof of strong hydrogen bonds. The intermolecular O···H and H···O contacts shown in Figure 4 provide a contribution of 22.9% to the HS of the C$_{24}$H$_{19}$N$_3$O$_5$S molecule. In Figure 4(c), the H···C/C···H intermolecular interactions comprise 22.9% of the total HS and represent two characteristic wings. The C–C contact includes only 4.3% of the total Hirshfeld surfaces area as shown in Figure 4(e) which is mainly assigned to π–π interaction. The N···H/H···N interactions comprising 3.7% of Hirshfeld surface, so appear weekly in the fingerprint plot. Figure 5 shows other contributions that are listed in decreasing order of one percent.

3.3. Vibrational assignments

We report in Table 1, both of experimental and computed vibrational frequencies with interrelated vibrational assignments and intensities. Also, we compare the experimental and calculated IR spectra plots in Figure 6. The calculated IR bands were carried out with the DFT with the functional B3LYP in conjunction with the 6-31G(d, p) basis set. Our C$_{24}$H$_{19}$N$_3$O$_5$S molecule consists of (52) atoms having 119 normal modes of vibrations. Also, the calculated vibrational assignments of the normal modes were performed on the basis of the Potential Energy Distribution (PED) and it has been calculated using the Vibrational Energy Distribution Analysis VEDA 4 program [30]. Usually, the calculated vibrational frequencies are higher than the corresponding experimental results. The
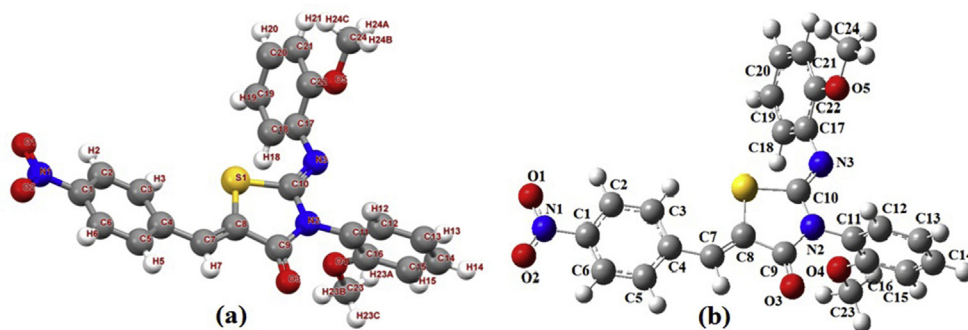

Figure 1. (a) Experimental structure and (b) optimized structure using B3LYP/6-31G(d, p) with the atomic numbering for C$_{24}$H$_{19}$N$_3$O$_5$S molecule.

computed wavenumbers values were scaled by scaling factor 0.9608 for DFT [31]. After scaling, the errors are minimized and the calculated vibrations show an excellent compatibility with the experimental values.

3.3.1. Benzene ring vibrations

The aromatic C–H stretching modes absorption in poly-substituted benzenes has been reported in the literature to be between 3000 and 3100 cm^{-1} [32]. Our results are in good accordance with those values. The C–H aromatic stretching mode was observed at 3058 cm^{-1} experimentally and computed at 3062 cm^{-1}. Our determination of the carbon–carbon stretching vibrations also demonstrates a good agreement between theory and experiments. The carbon–carbon stretching vibrations were observed in the FT-IR spectrum at 1587. 1513. 1504. 1461 cm^{-1} whereas the corresponding DFT calculated values are found to be 1580. 1571. 1542. 1475cm^{-1} respectively. The CCC in plane bending bands are expected in the literature to be between 1000 and 600cm^{-1} [33]. In this work, the CCC in plane bending bands were observed at 619cm^{-1} in the IR spectrum and calculated at 620cm^{-1} using the DFT method. The computed wavenumbers at 1036cm^{-1} are identified as CCC out of plane bending vibrations. The wavenumbers of CCCC in plane bending vibrations are computed at 672 and 671 with intensities 18.2 and 13.4 respectively.

3.3.2. Carbonyl vibrations

The carbonyl group wavenumber (C=O) stretching vibration is expected in the literature to be in the range 1710 cm^{-1} [34]. In our study, the experimental IR spectrum of carbonyl shows a strong band at 1721 cm^{-1} and the theoretically calculated value is 1738 cm^{-1}.

3.3.3. Methoxy group vibrations

In the FT-IR spectrum, the CH-stretching vibrations in OCH$_3$ group appeared at 2836 cm^{-1}. However the DFT calculations lead to values in the range of 3033 to 2897 cm^{-1}. The DFT calculated asymmetric stretching vibrations are shifted to the range 3026-2897 cm^{-1}. These values fit well with the results reported in the literature which are in the range 3034-2967 cm^{-1} and 2917-2904 cm^{-1} respectively for CH asymmetric and symmetric stretching vibrations [35]. The asymmetric and symmetric υO-C$_{Ar}$ stretching vibrations of methoxy group attached to an aromatic ring are given in the range 1310–1010 cm^{-1} [36,37]. In the

present work, the symmetric υ_sO-C$_{Ar}$ vibrations were observed in the medium FTIR band at 1255 cm^{-1}, 1042 cm^{-1} and calculated at 1258 and 1038 cm^{-1} by DFT method. The asymmetric υ_{as}O-C$_{Ar}$ vibrations were observed in the medium FTIR band at 1490, 1240 cm^{-1} and calculated at 1258 and 1489, 1482, 1241, 1232 cm^{-1} by the DFT method.

3.3.4. C–S group

In the literature, the C–S stretching vibration was observed between 800 cm^{-1} and 646 cm^{-1} for thiazole ring [38]. Our infrared experimental spectrum shows bands at 496 cm^{-1}, 680cm^{-1} which is assigned to asymmetric C–S stretching in the thiazole ring. The calculated values are predicted to be 17 cm^{-1} to 9 cm^{-1}respectively down than the experimental values.

3.3.5. C=N group

In this study, the C=N stretching vibration is observed at 1650 cm^{-1} in the IR spectrum and it is reported at 1640 cm^{-1} [39]. The others single C–N bands are cited in the Table 1.

3.3.6. NO$_2$ group

The NO$_2$ symmetrical stretching vibration is calculated at 1329 cm^{-1} using the DFT at the B3LYP level. The computed wavenumbers are found to be 834 and 638 cm^{-1} and they are assigned to N–O–N in plane bending vibrations of the nitro group. It was shown that the aromatic nitro compounds give strong peaks at the range of 1570–1485 cm^{-1} and 1370–1320 cm^{-1} due to asymmetric and symmetric stretching vibrations of the NO$_2$ group, respectively [13, 16].

3.4. Electronic properties

3.4.1. Frontier molecular orbital and UV–Vis spectral analysis

The lowest unoccupied molecular orbital (LUMO) and highest occupied molecular orbital (HOMO) are very important properties in quantum chemistry. LUMO is not occupied by electrons and produces the capacity to receive an electron. HOMO represents the ability to deliver an electron. The energy difference between them (HOMO and LUMO) is responsible on the chemical reactivity, optical polarizability and chemical hardness–softness of a molecule [40]. It is well known that molecules showing a small frontier orbital gap are easy to polarize and show a high
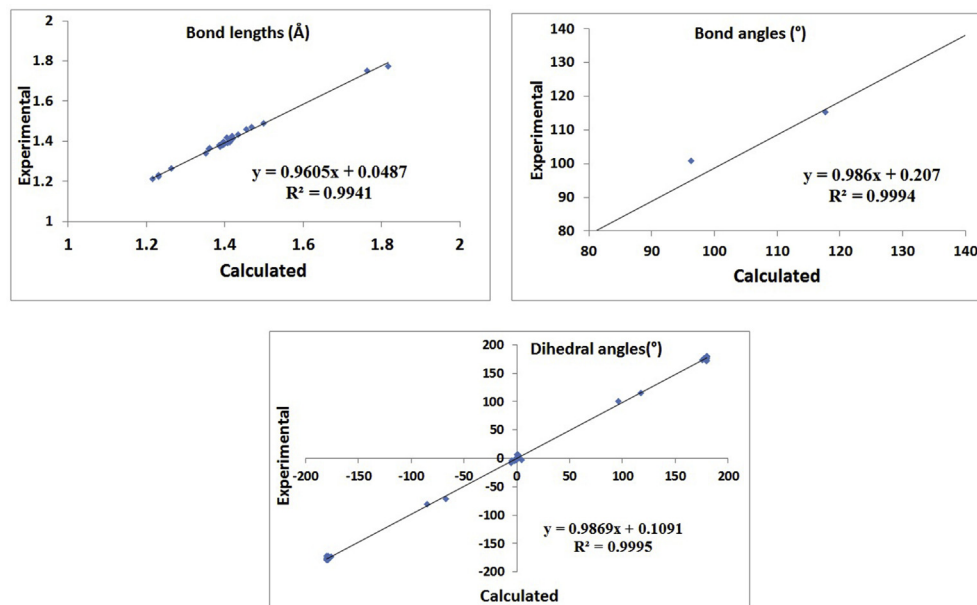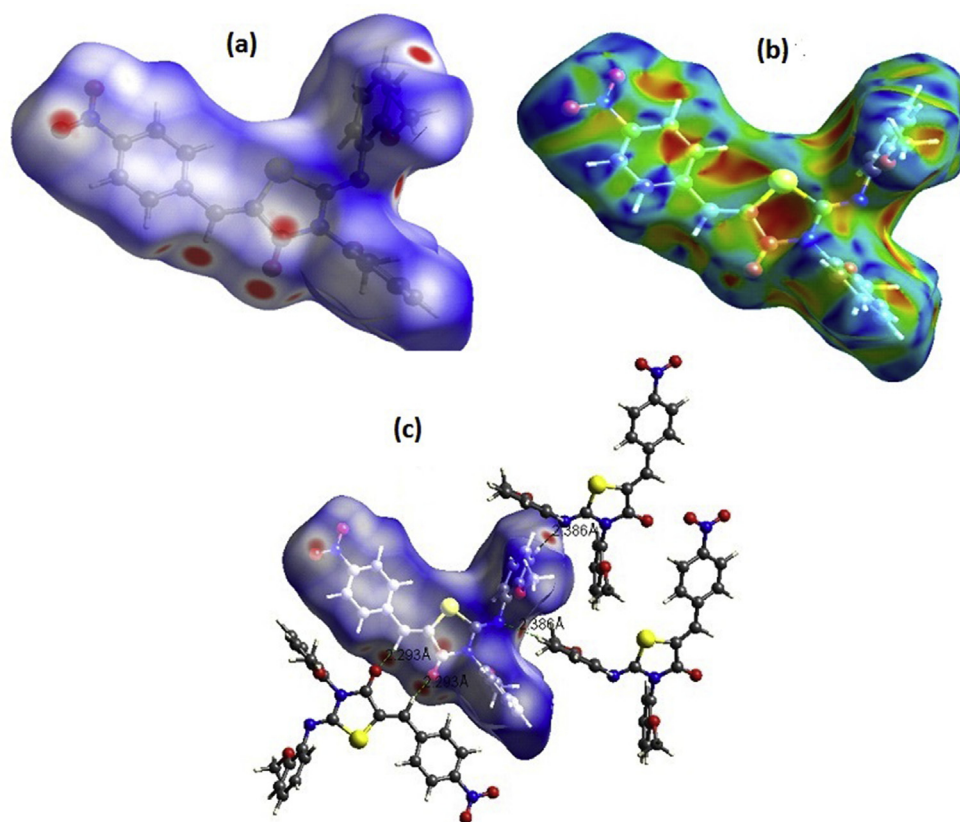

Figure 2. Correlation graphics of calculated and experimental bond lengths, bond angles and dihedral angles of C$_{24}$H$_{19}$N$_3$O$_5$S.

Figure 3. Hirshfeld surfaces for visualizing the intermolecular contacts of $C_{24}H_{19}N_3O_5S$: (a) d_{norm} Hirshfeld surface, (b) shape index and (c) d_{norm} selected intermolecular contacts.

chemical reactivity. They have low kinetic stability and can be seen as soft molecules [41]. In the present research work, we have used the DFT/B3LYP/6-31G (d,p) to calculate the energy values of the HOMO, LUMO, HOMO-1, LUMO+1, HOMO-2 and LUMO+2 (Figure 7). The energy values are given respectively by −5.828 eV, −2.858 eV, −6.404 eV, −1.585 eV, −6.434 eV and −0.782 eV. The value of gap energy excitation from HOMO to LUMO is calculated to be about 2.969 eV. It is clear from Figure 7 that the HOMO is located over the benzene related to methoxy group and LUMO, LUMO+1, LUMO+2 are located over the benzene related to the nitro group. Whereas, the HOMO-1 and HOMO-2 are delocalized over the entire molecule.

To compare with the experimental results of the UV-vis spectra, we have employed the TD-DFT method which provides an accurate value for the absorption wavelengths. The latter correlate to vertical electronic transitions computed on the ground state geometry. Calculations of the molecular orbital geometry show that the visible absorption maxima of this molecule correspond to the electron transition between frontier orbital such as translation from HOMO to LUMO. The UV-vis spectrum for our compound is measured in chloroform solvent in the region of 800-200 nm. This spectrum is also obtained using B3LYP level of TD-DFT with 6-31G(d, p) basis. We employed a fully optimized ground-state structure and TD-DFT/B3LYP/6-31G(d,p) calculations to compute the vertical excitation energies, oscillator strength and absorption wavelength. As per the Frank–Condon principle, the maximum absorption peak (λ max) in a UV spectrum corresponds to vertical excitation. Both of experimental and theoretical UV spectra are plotted in Figure 8.

The DFT calculations based B3LYP/6-31G(d, p) announce that theoretical UV-Vis spectrum shows two-absorption peaks at 495 nm and 388 nm with oscillators strengths $f = 0.0445$ and 0.3692 respectively. Also, we can observe absorption peaks observed in high energy region at 468

nm and 360 nm from the UV-vis absorption spectrum. They are assigned as n → π* and π → π* respectively, which are in excellent accord with the DFT calculated maximum values.

3.4.2. Global reactivity descriptors

Global chemical reactivity descriptors (GCRD) parameters are a good indication to highlight the relationship between chemical reactivity and strength of structure. GCRD parameters can be obtained using the following equations:

$$\eta = 1/2 \, (E_{LUMO} - E_{HOMO}); \; \mu = 1/2 \, (E_{LUMO} + E_{HOMO}); \; S = 1/2 \, \eta \, ;$$

$$\chi = -\frac{1}{2}(E_{LUMO} + E_{HOMO}); \; \omega = \frac{\mu^2}{2\eta}; \; E_A = -E_{LUMO} \text{ and } I_P = -E_{HOMO}$$

where η is the global hardness, μ is the chemical potential, S is the global softness, χ is the electronegativity, ω is the electrophilicity index.

According to the Table 2, the chemical hardness value (η) was calculated at 1.485 eV using functional B3LYP in conjunction with the 6-31G(d,p) basis set, indicating that charge transfer occurs within the molecule. The electrophilic conduct of the molecule is confirmed by the global electrophilic index (ω) which has a value of 17.732 eV. On the additional hand, the chemical stability of the titer molecule is expressed by the chemical potential value (μ) which is −7.257 eV.

3.4.3. Optical band gap

The gap energy between HOMO and LUMO can be measured experimentally by spectroscopic methods and conductivity [42]. The UV-visible spectrum can be used as a simple and straight forward technique to accurately estimate the gap energy for π-conjugated materials.
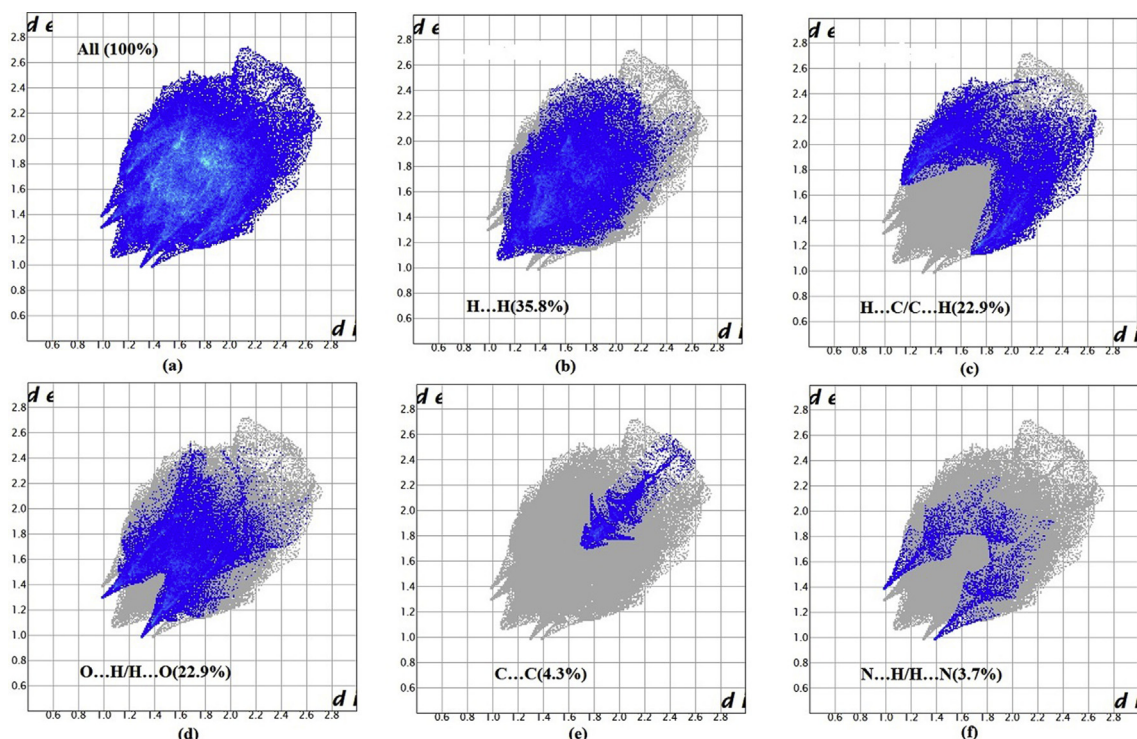
Figure 4. Two-dimensional fingerprint plots displaying contributions of different types of interactions: (a) all intermolecular contacts, (b)H–H contacts, (c) C–H/H–C contacts, (d) O–H/H–O contacts, (e) C–C contacts and (f) N–H/H–N contacts.
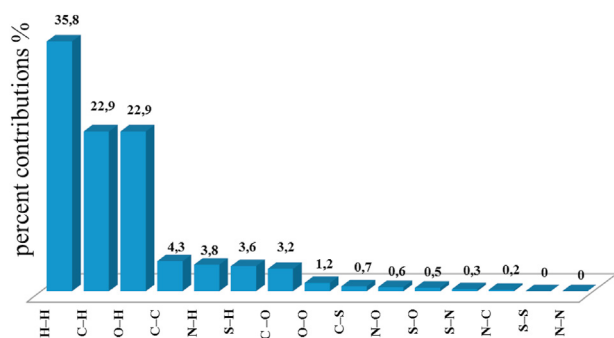
Figure 5. Quantitative results of different intra- and intermolecular interactions contributing to the HS.

From UV-visible spectrum, the optical gap can be estimated according to equation (*I*).

$$E_g(eV) = h.\upsilon = h.\frac{C}{\lambda_{Eg}} \approx \frac{1240}{\lambda_{Eg}(nm)} \qquad (I)$$

The optical gap, E_g, is expressed in eV and λE_g is the absorption band expressed in nm obtained from the intersection of the two lines as shown in Figure 9 [43].

From the experimental UV-visible spectrum, the wavelength is λE_g = 423 nm, so the optical gap value is equal to 2.931 eV, this value is close to the band gap value calculated by DFT, 2.969 eV. This work has shown that UV-Vis analysis in the CHCl₃ solution can be used as an easy and direct technique to accurately estimate the band gap energy of conjugated π organic compounds, which is a crucial property to evaluate the optical and conductive properties of a material. The experimental value approach and calculated by the functional B3LYP and the bases 6-31G(d, p) confirms the correct choice of models of calculations.

3.4.4. ^1H and ^{13}C NMR spectra

The use of ^{1}H and ^{13}C NMR spectroscopy is one of the important tools in characterizing molecules. The ^{1}H and ^{13}C NMR spectra of the C₂₄H₁₉N₃O₅S molecules are performed by Bruker Ac DPX-200 (300 MHz) spectrometer in CDCl₃ as solvent. The experimental results are compared to the GIAO (gauge-independent atomic orbital) ^{1}H and ^{13}C chemical shift values. The latter were computed from B3LYP functional and 6-31G(d, p) basis set. The geometry of C₂₄H₁₉N₃O₅S together with that of tetramethylsilane (TMS) were fully optimized. For comparing the theoretical ^{1}H NMR chemical shifts of our compound with the experimental data, the ^{1}H and ^{13}C NMR chemical shifts were converted to the TMS scale by subtracting the calculated absolute chemical shielding of TMS with values of 31.75 ppm (^{1}H) and 192.82 ppm (^{13}C) for B3LYP/6-31G (d, p). Experimental results together with the theoretical one are gathered in Table 3.

The formation of the C₂₄H₁₉N₃O₅S was clearly proved by the appearance of singlet two peaks of OCH₃ at 3.72 ppm and 3.82 ppm. Note that the chemical shift of the protons of the methoxy group (O–CH3) is deblinded, following the delocalization of the free doublet of oxygen generated by the group imino (C=N). The corresponding theoretical values of the mentioned peaks are observed at 3.46–3.90 ppm and 3.62–3.97 ppm, respectively. In the ^{1}H NMR spectrum, the aromatic proton signals appear as a mutiplet at 6.79–8.18 ppm regions whereas the calculated values are observed at 6.63–8.44 ppm. The peak of methine proton exo-cyclic appeared at 7.73 ppm experimentally and observed at 7.64 ppm from computations. Signals exhibited at 8.42 and 8.44 ppm might be attributed to H6, H2 protons respectively close to the nitro group. While the ^{13}C NMR spectra of the title compound showed the presence of carbonyl carbon atoms at 165.69 ppm. This value is observed at 160.50 ppm theoretically. Carbons of methoxy groups (C23 and C24) are calculated at 53.88 ppm and 53.55 ppm respectively, these values are observed at 55.98 ppm and 55.90 ppm experimentally. As reported by these results, the calculated chemical shifts are in good compliance with

Table 1. Comparison of the experimental and calculated vibrational values and the proposed assignments of compounds.

Mode no.	Experimental wavenumbers (cm^{-1})	Theoretical wavenumbers (cm^{-1}) (B3LYP/6-31G(d,p))			Assignments with PED ($\geq$10 %)
		Unscaled	Scaled	I_{IR}	
118		3248	3120	1.4	υ_{sCH} (ring 1) (91)
117		3247	3120	0.8	υ_{sCH} (ring 1) (84)
116		3229	3102	8.5	υ_{asCH} (ring 2) (13) + υ_{sCH} (ring 2) (73)
115		3227	3100	4.6	υ_{sCH} (ring 1) (90)
114		3225	3098	14.2	υ_{sCH} (ring 3) (85)
113		3219	3093	12.0	υ_{asCH} (ring 2) (73) + υ_{sCH} (ring 2) (18)
112		3210	3085	16.4	υ_{asCH} (ring 3) (10) + υ_{sCH} (ring 3) (84)
111		3205	3080	14.8	υ_{sCH} (ring 2) (95)
110		3200	3074	4.5	υ_{sCH} (ring 1) (97)
109		3198	3072	16.4	υ_{asCH} (ring 3) (93)
108		3190	3065	4.2	υ_{asCH} (ring 2) (86)
107	3058	3187	3062	0.2	υ_{asCH} (ring 3) (88)
106		3169	3045	0.9	υ_{sC7H7} (99)
105	3033	3156	3033	15.8	υ_{sCH} (CH3)1 (91)
104		3150	3026	19.4	υ_{asCH} (CH3)2 (99)
103	2994	3091	2969	29.6	υ_{sCH} (CH3)1 (100)
102	2942	3078	2957	38.0	υ_{sCH} (CH3)2 (98)
101		3024	2906	54.4	υ_{sCH} (CH3)1 (91)
100	2836	3016	2897	71.4	υ_{asCH} (CH3)2 (20) + υ_{sCH} (CH3)2 (79)
99	1721	1809	1738	87.7	υ_{sO3C9} (76)
98	1650	1745	1677	872.0	υ_{sO3C9} (10) + $\upsilon_{asN3C10}$ (76)
97	1606	1669	1604	122.3	υ_{asC7C8} (53)
96		1660	1595	49.7	υ_{asCC} (ring2) (62)
95		1659	1594	35.3	υ_{sCC} (ring1) (57)
94	1587	1644	1580	22.1	υ_{sCC} (ring1) (42)
93		1644	1579	83.8	υ_{as} CC(ring1) (21) + υ_{as} CC(ring2) (20)
92		1643	1579	51.2	υ_{sCC} (ring2) (34) + υ_{asCC} (ring1) (14)
91	1513	1635	1571	6.3	υ_{asCC} (ring3) (52) + δ_{CCC} (ring 3) (12)
90	1504	1605	1542	120.0	υ_{asCC} (ring 1) (61)
89	1490	1550	1489	109.1	υ_{asOC} (ring 2) (11) + δ_{HCC}(ring 2) (38) + δ_{CCC}(ring 2) (10)
88		1542	1482	70.6	υ_{asOC} (ring3) (10) + δ_{HCC} (ring3) (29) + δ_{CCC} (ring3) (19)
87	1461	1535	1475	14.7	υ_{asCC}(ring 1) (10) + δ_{HCC} (ring 1) (50)
86		1518	1459	51.2	δ_{HCH} (CH3) 2 (68) + τ_{HCOC}(methoxy2) (22)
85		1517	1458	44.0	δ_{HCH} (CH3) 1 (66)+ τ_{HCOC} (methoxy1) (19)
84		1506	1447	12.3	υ_{asCC}(ring2) (22)+ δ_{HCC} (ring2) (54)
83		1505	1446	4.8	δ_{HCH} (CH3) 2 (74)+ τ_{HCOC} (methoxy2) (24)
82		1505	1446	4.8	δ_{HCH} (CH3) 1 (73) + τ_{HCOC} (methoxy1) (24)
81	1436	1499	1440	2.7	υ_{asCC} (ring3) (17) + $\delta_{HCH(CH3)}$ 2 (62)
80		1481	1423	18.9	δ_{HCC} (ring2) (75)
79	1410	1479	1421	27.4	υ_{sCC}(ring3) (14)+ $\delta_{HCH(CH3)}$ 2 (67)
78	1376	1453	1396	13.1	υ_{sCC}(ring1) (48) + δ_{HCC}(ring1) (26)
77		1395	1340	58.8	υ_{sN2C11} (65)
76	1336	1387	1333	208.2	υ_{sCC}(ring1) (28) + δ_{H7C7C4} (31)
75		1384	1329	982.9	υ_{sON} (nitro) (56)
74		1358	1305	42.4	υ_{sCC} (ring2) (65)
73		1357	1303	22.6	υ_{sCC} (ring3) (55)
72		1356	1303	45.8	υ_{asCC}(ring3) (12) + δ_{HCC}(ring1) (22) + δ_{H7C7C4}(15)
71	1290	1329	1277	23.7	δ_{HCC} (ring1) (49)
70	1280	1321	1270	69.2	υ_{as} N3C17 (43) + δ_{HCC}(ring3) (12)
69		1318	1266	80.7	υ_{asOC}(methoxy1) (22) + δ_{HCC}(ring2) (34)
68	1255	1310	1258	123.8	υ_{asCC}(ring3) (10) + υ_{OC}(ring3)s (18) + δ_{HCC}(ring3) (39)
67	1240	1291	1241	154.7	υ_{asOC}(ring2) (17) + δ_{HCC}(ring2) (18)
66		1283	1232	63.1	υ_{sOC}(ring3) (21) + υ_{asOC}(methoxy2) (11)
65		1252	1203	45.52	υ_{sC4C7} (32)
64	1184	1218	1170	8.4	γ_{HCC}(ring1) (61)
63	1172	1215	1167	23.5	$\delta_{HCH(CH3)1}$ (12) + τ_{HCOC} (methoxy1) (41) + τ_{HCOC} (methoxy2) (10)

Table 1 (*continued*)

Mode no.	Experimental wavenumbers (cm^{-1})	Theoretical wavenumbers (cm^{-1}) (B3LYP/6-31G(d,p))			Assignments with PED (≥10 %)
		Unscaled	Scaled	I_{IR}	
62	1160	1214	1166	4.1	δ_{HCH} (15) + τ_{HCOC} (13) + τ_{HCOC} (44)
61		1194	1147	160.7	υ_{sN3C17} (10)
60		1192	1145	10.3	δ_{HCC} (ring2) (80)
59		1190	1143	25.8	$\upsilon_{sCC(ring3)}$ (10) + $\delta_{HCC(ring3)}$ (65)
58		1182	1136	68.8	υ_{sN2C11} (31)
57		1179	1133	0.9	$\delta_{HCH(CH3)2}$ (25) + $\tau_{HCOC(methoxy2)}$ (73)
56		1178	1132	0.6	$\delta_{HCH\ (CH3)1}$ (25) + $\tau_{H\ COC(methoxy1)}$ (73)
55	1106	1144	1100	29.9	δ_{HCC} (ring1) (45)
54		1140	1095	101.3	υ_{asCC} (ring3) (10)
53	1051	1131	1087	94.4	$\upsilon_{asCC(ring1)}$ (56) + $\delta_{HCC\ (ring1)}$ (11) + $\gamma_{HCC(ring1)}$ (12)
52	1042	1080	1038	40.7	$\upsilon_{sOC\ (methoxy2)}$ (38) + $\delta_{HCC\ (ring3)}$ (13)
51		1078	1036	20.9	$\upsilon_{sCC(ring2)}$ (47) + $\delta_{HCC\ (ring2)}$ (11) + $\gamma_{CCC(ring2)}$ (10)
50	1022	1064	1023	10.1	υ_{sCC} (ring2) (59)
49		1064	1022	36.2	$\upsilon_{sCC(ring2)}$ (66)
48		1059	1017	52.4	$\upsilon_{asCC(thiazol)}$ (20) + $\delta_{CCC(ring1)}$ (10)
47		1029	988	0.4	$\delta_{HCC(ring1)}$ (14) + $\delta_{CCC\ (ring1)}$ (77)
46		993	954	0.1	$\tau_{H38C3C4C7}$ (79)
45		981	943	1.6	$\tau_{HCCC\ (ring1)}$ (59) + $\tau_{CCCC(ring1)}$ (11)
44	935	979	941	0.1	$\tau_{HCCC(ring2)}$ (70) + $\tau_{CCCC(ring2)}$ (10)
43	929	966	928	0.1	$\tau_{HCCC(ring3)}$ (65) + $\tau_{CCCC(ring3)}$ (27)
42	913	943	906	1.4	$\tau_{HCCC(ring2)}$ (10) + $\tau_{HCCC\ (ring2)}$ (76)
41		941	904	15.1	$\tau_{H7C7C4C5}$ (71)
40		927	891	10.6	τ_{HCCC} (ring3) (87)
39	871	909	874	2.6	δ_{C7C8C9} (14)
38	850	874	839	94.6	$\delta_{N3C10N2}$ (12)
37		868	834	21.2	υ_{sN1C1} (24) + $\delta_{ONO(nitro)}$ (33)
36		863	829	17.1	$\tau_{HCCC(ring1)}$ (72)
35	826	860	826	2.5	$\tau_{HCCC(ring2)}$ (57)
34	817	855	822	2.7	$\tau_{HCCC(ring3)}$ (71)
33		838	805	70.7	$\delta_{CCC(ring3)}$ (20)
32		838	805	1.2	$\tau_{HCCC(ring1)}$ (88)
31	770	805	774	0.1	$\delta_{CCC(ring2)}$ (10)
30		787	756	13.1	$\delta_{CCC(ring1)}$ (14)
29	749	777	746	13.3	$\tau_{HCCC(ring2)}$ (17)
28		763	733	17.3	$\tau_{CCCC(ring1)}$ (59)
27		763	733	22.8	$\tau_{HCCC(ring2)}$ (10) + $\tau_{HCCC(ring2)}$ (40) + $\gamma_{OCCC(ring2)}$ (12)
26	731	762	732	57.7	$\tau_{HCCC(ring3)}$ (72)
25		740	711	4.3	$\tau_{HCCC(ring3)}$ (12) + $\tau_{CCCC(ring3)}$ (51)
24		734	705	2.2	$\gamma_{ONCC(thiazol)}$ (66)
23	689	723	695	7.9	$\tau_{CCCC(ring2)}$ (16) + $\gamma_{OCCC(ring2)}$ (12)
22		700	672	18.2	δ_{C4C7C8} (10) + $\tau_{CCCC(ring2)}$ (41)
21	680	698	671	13.4	$\upsilon_{as\ SC\ (thiazol)}$ (12) + δ_{C4C7C8} (21) + $\tau_{CCCC\ (ring1)}$ (18)
20	650	664	638	19.1	$\delta_{CCC(ring1)}$ (11) + $\delta_{ONO(nitro)}$ (11) + $\delta_{CCC\ (ring2)}$ (12)
19	619	646	620	4.8	$\delta_{CCC(ring1)}$ (14) + $\delta_{CNC\ (thiazol)}$ (21)
18		631	606	0.4	$\delta_{CCC(ring1)}$ (37) + $\delta_{CNC\ (thiazol)}$ (12)
17	595	614	589	5.2	$\delta_{CCC(ring3)}$ (25) + $\tau_{N3C10N2C11}$ (13)
16		609	585	33.6	$\delta_{SCC(thiazol)}$ (13)
15		600	577	1.7	$\tau_{N3C10N2C11}$ (25)
14	559	575	553	6.4	$\delta_{C18C17N3}$ (10) + $\delta_{O5C22C21}$ (20) + $\delta_{COC\ (methoxy2)}$ (17)
13		571	549	14.3	$\delta_{O4C16C15}$ (10) + $\tau_{HCCC(ring3)}$ (10)
12		565	543	26.5	$\delta_{CCC(ring1)}$ (19)
11	530	559	537	0.2	$\tau_{HCCC\ (ring2)}$ (14) + $\tau_{CCCC(ring2)}$ (32) + $\gamma_{O4C11C15C16}$ (16)
10	516	537	516	5.4	$\tau_{CCCC(ring1)}$ (11) + $\tau_{C4C7C8C9}$ (11) + $\tau_{CCCC(ring2)}$ (19)
9		533	512	0.9	δ_{C1N1O1} (50) + $\tau_{CCCC(ring2)}$ (10)
8		530	509	2.7	δ_{C1N1O2} (20) + $\tau_{CCCC(ring2)}$ (18)
7		518	498	1.4	$\delta_{CCC(ring3)}$ (26)
6	496	499	479	14.7	$\upsilon_{asSC(thiazol)}$ (21) + $\delta_{CCN(thiazol)}$ (15)
5	469	481	462	3.8	γ_{O3C8C9} (13) + $\gamma_{O4C11C15C16}$ (15) + $\gamma_{N2C16C12C11}$ (10)

Table 1 (*continued*)

Mode no.	Experimental wavenumbers (cm^{-1})	Theoretical wavenumbers (cm^{-1}) (B3LYP/6-31G(d,p))			Assignments with PED ($\geq$10 %)
		Unscaled	Scaled	I_{IR}	
4	448	460	442	0.6	$\tau_{CCCC(ring3)}$ (50)
3	433	447	429	1.2	$\tau_{CCCC(ring1)}$ (54)
2	408	419	402	0.6	τ_{HCCC} (ring1) (11) + $\tau_{CCCC(ring1)}$ (62)
1		417	400	18.4	υ_{asN1C1} (24) + $\delta_{CCC(ring1)}$ (19)

υ: Stretching; s: symmetric; as: asymmetric; δ: in plane bending; γ: out of plane bending; τ: twisting; ρ: rocking. Scaled frequencies are in units of cm^{-1}, I_{IR} infrared intensities are in units of km mol^{-1}.
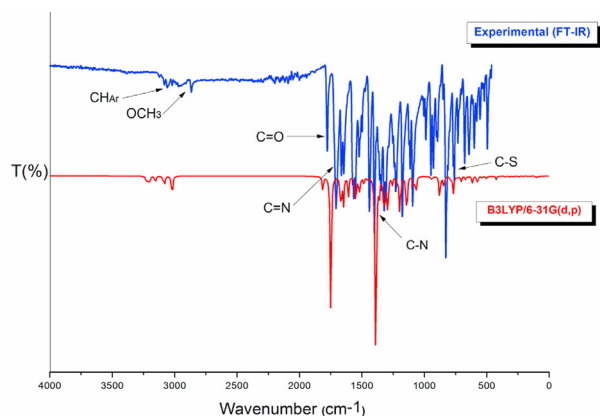

Figure 6. Comparison between experimental and calculated FT-IR spectra of using B3LYP/6-31G(d, p) approach.

Figure 8. UV-visible theoretical spectrum and experimental in chloroform solvent.

the experimental data. Furthermore, the small shifts might be due to the molecular environmental change.

3.4.5. Natural bond orbital analysis

NBO analysis provides useful information about intra-and intermolecular bonding. Also, it gives details dealing with interactions in connection with bonds, and can be seen as a convenient tool for exploring charge transfer within molecular systems. The NBO calculations were performed using NBO program [44] as implemented in the Gaussian03 software package. Again, we employed DFT/B3LYP/6–31G(d,p) approach to draw a picture about the intra-molecular hybridization and delocalization of electron density within the molecule. The π-electron delocalization is maximum around π (C1–C6).π (C2–C3) and π (C4–C5) distributed to π* anti-bonding of π* (C2–C3), π* (C4–C5) and π* (C1–C6)

with a stabilization energy of about 17.29–23.93 kcal mol^{-1} as shown in Table 4. The analysis for the title compound shows strong intra-molecular hyper-conjugated interactions π (C11–C12) shows strong stabilization energies of 21.96 kcal mol^{-1} and 16.17 kcal mol^{-1} with π* (C16–C15) and π* (C14–C13) respectively and π (C16–C15) shows comparable stabilization energy of 17.05 kcal mol^{-1} and 22.38 kcal mol^{-1} with π* (C11–C12) and π* (C14–C13) respectively. This reveals that (C16–C15) prefers to be acceptor than to be a donor with (C11–C12). Conversely π (C14–C13) involves interaction with π* (C11–C12) and π* (C16–C15) with stabilization energy of 23.23 kcal mol^{-1} and 17.31 kcal mol^{-1} indeed it gives the explanation that (C11–C12) prefers to be an acceptor with (C14–C13). The important intra-molecular hyper--conjugated interactions are: (N3–C10) from (S1) of n2 (S1)→π*
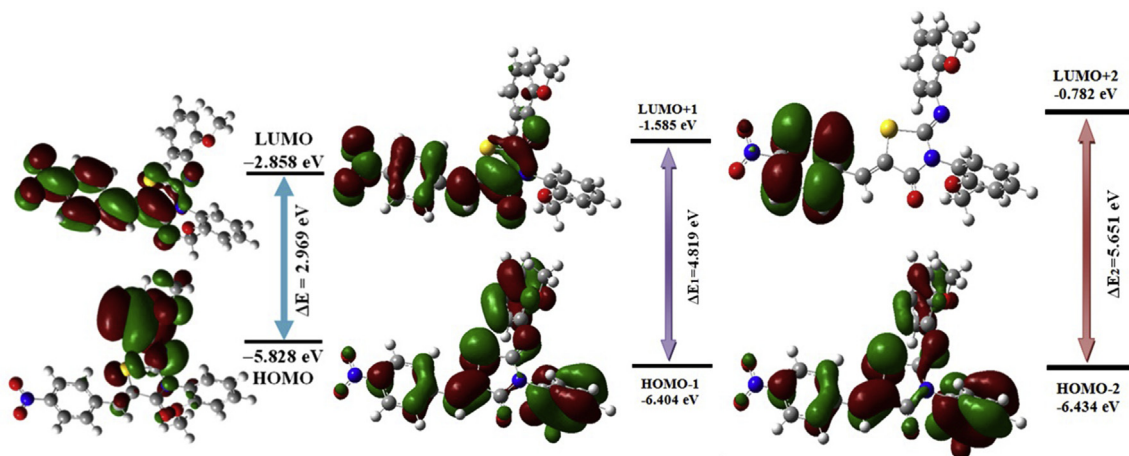

Figure 7. Molecular orbital surfaces and energy levels for the HOMO, LUMO, HOMO-1, LUMO+1, HOMO-2 and LUMO+2 of the C$_{24}$H$_{19}$N$_3$O$_5$S molecule computed at B3LYP/6-31G(d, p) level.

(N3–C10).(C9–N2)from (O3) of n2 (O3)→σ* (C9–N2).(C16–C15) from (O4) of n2 (O4)→π* (C16–C15) and (C22–C21) from (O5) of n2 (O5)→π* (C22–C21) with electron densities 1.76144, 1.84216, 1.83710, 1.83777 e and stabilization energies 21.91, 29.32, 31.93, 30.98 kcal mol^{-1}. The energy value of the interactions π* (C16–C15) →π* (C14–C13) is 281.71 kcal mol^{-1}, indicating that these interactions produce a great stabilization in the molecule. The delocalization of electrons due to n3 (O2) →π* (O1–N1), n1 (N2)→π* (C9–O3) and n1 (N2) →π* (N3–C10) having the highest intra-molecular charge transfer interaction (ICT) energies (E$^{(2)}$) of 163.38,54.70 and 44.18 kcal mol^{-1} respectively.

In Table 5, σ (C1–C6) orbital with 1.97633 electrons has 51.03% C1 character in a sp$^{1.65}$ hybrid and has 48.97% C6 character in a sp$^{1.98}$ hybrid. The sp$^{1.65}$ hybrid on C has 62.29% p character and sp$^{1.98 hybrid}$ on C have 66.46 % p character $C_{24}H_{19}N_3O_5S$ molecule. The σ (C2–C3) orbital with 1.97569 electrons has 50.19 % C2 character in a sp$^{1.80}$ hybrid and has 49.81 % C3 character in a sp$^{1.83}$ hybrid. The sp$^{1.80}$ hybrid on C has 64.31 % p-character and the sp$^{1.83}$ hybrid on C has 64.58 % p-character. The bonding orbital for σ* (C8–S1) with 0.03789 electrons has 45.86 % C8 character in a sp$^{2.76}$ hybrid and has 54.14 % S26 character in a sp$^{4.80}$ hybrid orbital.

3.4.6. Molecular electrostatic potential (MEP)

The distribution of charges (either positive or negative) in molecules/crystal can be understood from calculation of the molecular electrostatic potential (MEP) [45]. The electrostatic potential is important in the study of intermolecular interactions of molecular systems and it can be obtained from the experimental X-ray diffraction data and the *ab-initio* theoretical calculations [46, 47]. To study the reactive sites of our molecule, the molecular electrostatic potential was computed from the optimized geometry using B3LYP/6-31G(d, p) functional and its surface map is shown in Figure 10.

As can be seen in Figure 10, the different values of the electrostatic potential of our molecule are represented by different colors in the ranges -0.05072 and +0.05072. The electrophilic reactivity visualized by the red color indicates the negative regions of the molecule, the nucleophilic reactivity visualized in blue indicates the positive regions of the molecule and the green color symbolizes the regions of neutral electrostatic potential. The negative regions of the electrostatic molecular potential (MEP) are mainly localized on the carbonyl group (C=O), the nitro group (NO$_2$) and the imino group (C=N) indicating the possible sites of electrophilic reactivity due to the property electronegative of oxygen and nitrogen atoms. Positive regions of the MEP map that are localized around phenyl and methyl groups indicate possible sites of nucleophilic attack. The thiazole group is surrounded by a neutral electrostatic potential.

The electrostatic distribution previously studied can be confirmed with the orientation of the molecular dipole moment. The dipole moment vector depends mainly on the position of substituents. From DFT calculation the orientation of the molecular dipole moment for the title

compound is represented in Figure 11 with calculated value is 6.47D.This orientation corroborates the MEP distribution previously discussed.
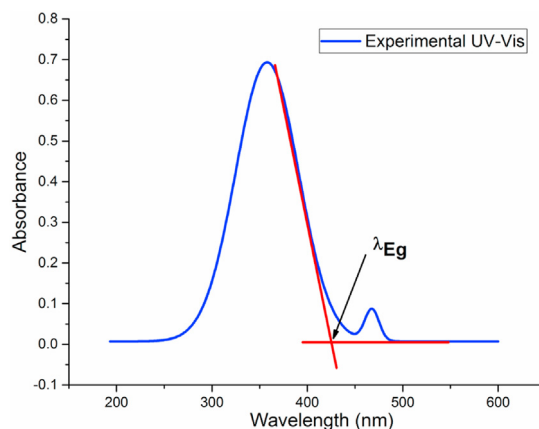
4. Molecular docking methodology

Molecular docking has now become an increasingly significant tool for drug discovery and docking small molecular systems into binding site of DNA, enzymes and proteins. Presently Chemical Computing Inc., MOE: 2017 software was used to import, optimize and dock the molecular structure of $C_{24}H_{19}N_3O_5S$ into binding pockets of two acetylcholinesterase and butylcholinesterase enzymes. Molecular structures of PB were imported and optimized using MM force field and entered into MOE database by selecting entries. The optimized X-ray crystallographic structure of Acetylcholinesterase (PDB ID: 2X8B), XRD resolution of 2.95 Å and Butyrylcholinesterase (PDB ID: 1XLW), XRD resolution of 2.1 Å was obtained from PDB [48, 49] and imported to MOE visualizer to arrange for molecular docking simulation. Docking preparation includes removal of water molecules from XRD structure and protonation of both enzymes to lowest energy state using the MOPAC 7.0 and amber force field. All water molecules were removed macromolecular system. Before docking simulations. After pre-preparation of 2X8B and 1XLW and $C_{24}H_{19}N_3O_5S$ molecule, XRD structure of 2X8B and 1XLW was allowed to dock with the optimized molecule of $C_{24}H_{19}N_3O_5S$ molecules under default parameters with RMS gradient of 0.01 kcal mol. Several conformations of docked poses were obtained based on minimum free energy values. The docked conformation fitting into pockets of binding pockets of acetylcholinesterase and butylcholinesterase having minimum energy and maximum stability was selected as a final docking pose [50, 51].

4.1. DNA-binding studies by molecular docking

Molecular docking is widely a probed computational method to determine covalent and non-covalent interactions between small molecules and macromolecules i.e.; enzymes, proteins and DNA. It is most suitable and reliable methods for structure-based and ligand-based drug designing [51]. Computational screening of biological and biochemical molecules before experimental synthesis can be facile and cost effect way [45, 50, 51].

Present section involves $C_{24}H_{19}N_3O_5S$ molecule probed into interaction study ofacetylcholinesterase (PDB ID: 2X8B), and Butyrylcholinesterase (PDB ID:1XLW) using molecular docking methodology. The lowest energy docked pose of the $C_{24}H_{19}N_3O_5S$ molecule is presented in Figure 12. Ligplot (right side of Figure 12A/C) are demonstrating interaction profiles revealed that blue blurred regions indicate direct exposure of $C_{24}H_{19}N_3O_5S$ molecule to the residues of acetylcholinesterase and Butyrylcholinesterase. Dotted lines in the shape of curves

Table 2. Calculated quantum chemical reactivity descriptors for $C_{24}H_{19}N_3O_5S$ molecule.

Parameters	B3LYP/6-31G(d.p)
E_{HOMO} (eV)	-5.828
E_{LUMO} (eV)	-2.858
$E_{HOMO} - E_{LUMO}$ (eV)	2.970
IP (eV)	5.828
EA (eV)	2.858
χ (eV)	7.257
μ	-7.257
η (eV)	1.485
S	0.743
ω	17.732

Figure 9. Schematic representation of experimental UV-Vis spectrum and the band gap energy estimation.

Table 3. Comparison of the experimental and calculated NMR values.

ATOMS	EXP (δ ppm)	B3LYP/6-31G(d,p)	ATOMS	EXP (δ ppm)	B3LYP/6-31G(d,p)
H2	8.18	8.44	C1	147.46	143.76
H3	7.54	7.68	C2	121.85	121.19
H5	7.54	7.46	C3	126.07	124.55
H6	8.18	8.42	C4	140.12	136.90
H7	7.73	7.64	C5	130.38	130.77
H12	7.52	7.38	C6	121.21	120.56
H13	7.38	7.11	C7	126.93	125.13
H14	7.52	7.47	C8	131.12	131.18
H15	6.90	6.78	C9	165.69	160.50
H18	7.01	6.82	C10	150.09	145.91
H19	7.10	6.93	C11	124.17	123.21
H20	7.33	7.14	C12	129.85	127.81
H21	6.79	6.63	C13	120.98	116.28
H23A	3.82	3.97	C14	127.44	126.45
H23B	3.82	3.64	C15	112.59	107.15
H23C	3.82	3.62	C16	155.02	151.21
H24A	3.72	3.90	C17	137.33	135.07
H24B	3.72	3.60	C18	120.99	116.63
H24C	3.72	3.46	C19	120.97	115.82
			C20	123.15	121.35
			C21	112.24	106.80
			C22	150.65	147.15
			C23	55.98	53.88
			C24	55.90	53.55

Table 4. Natural bond analysis of the $C_{24}H_{19}N_3O_5S$ molecule.

Donor (i)	ED/e	Acceptor (j)	ED/e	E(2) (kcal/mol)	E(j)–E(i) (a.u.)	F(i.j) (a.u.)
π (C1–C6)	1.63134	π* (C2–C3)	0.27849	20.15	0.29	0.070
π (C1–C6)	1.63134	π* (C4–C5)	0.37850	18.51	0.29	0.065
π (C2–C3)	1.66209	π* (C1–C6)	0.38966	19.46	0.28	0.066
π (C2– C3)	1.66209	π* (C4–C5)	0.37850	20.25	0.28	0.068
π (C4–C5)	1.58603	π * (C1–C6)	0.38966	23.93	0.27	0.072
π (C4–C5)	1.58603	π* (C2–C3)	0.27849	17.29	0.28	0.064
π (C11–C12)	1.70924	π* (C16–C15)	0.38405	21.96	0.28	0.072
π (C11–C12)	1.70924	π* (C14–C13)	0.33235	16.17	0.29	0.062
π (C16 – C15)	1.65449	π* (C11–C12)	0.35331	17.05	0.29	0.063
π (C16–C15)	1.65449	π* (C14–C13)	0.33235	22.38	0.29	0.073
π (C14–C13)	1.67663	π* (C11–C12)	0.35331	23.23	0.28	0.073
π (C14–C13)	1.67663	π* (C16–C15)	0.38405	17.31	0.27	0.062
π (C17–C18)	1.69087	π* (C22–C21)	0.38608	19.64	0.28	0.068
π (C17–C18)	1.69087	π* (C19–C20)	0.34132	18.09	0.29	0.066
π (C22–C21)	1.68124	π*(C17–C18)	0.37690	17.25	0.29	0.064
π (C22–C21)	1.68124	π* (C19–C20)	0.34132	20.50	0.30	0.070
π (C19–C20)	1.69328	π* (C17–C18)	0.37690	20.74	0.28	0.069
π (C19–C20)	1.69328	π* (C22–C21)	0.38608	17.97	0.27	0.06
π (C4–C5)	1.58603	π* (C7–C8)	0.21467	18.46	0.28	0.067
π (C7–C8)	1.84225	π* (C4–C5)	0.37850	11.77	0.31	0.057
π (C7–C8)	1.84225	π* (C9–O3)	0.28608	18.33	0.30	0.068
σ (C7–H7)	1.96338	σ* (C8–S1)	0.03789	10.14	0.71	0.076
π (O1–N1)	1.98523	n3 (O2)	1.44613	12.20	0.18	0.078
π (C1–C6)	1.63134	π* (O1–N1)	0.63210	28.36	0.15	0.062
n2(O2)	1.89839	σ* (C1–N1)	0.10337	12.51	0.57	0.076
n2 (O2)	1.89839	σ* (O1–N1)	0.05676	19.23	0.71	0.105
n3(O2)	1.44613	π* (O1–N1)	0.63210	163.38	0.14	0.139

Table 4 (*continued*)

Donor (i)	ED/e	Acceptor (j)	ED/e	E(2) (kcal/mol)	E(j)–E(i) (a.u.)	F(i,j) (a.u.)
n2 (O1)	1.89839	σ* (C1–N1)	0.10337	12.52	0.57	0.076
n2 (O1)	1.89839	σ* (O2–N1)	0.05677	19.24	0.71	0.105
n2 (S1)	1.76144	π* (C7–C8)	0.21467	21.91	0.28	0.070
n2 (S1)	1.76144	π* (N3–C10)	0.27332	21.91	0.28	0.070
n2 (O3)	1.84216	σ* (C8–C9)	0.08180	21.74	0.65	0.108
n2 (O3)	1.84216	σ* (C9–N2)	0.09450	29.32	0.67	0.127
n2 (O4)	1.83710	π* (C16–C15)	0.38405	31.93	0.34	0.099
n1 (N3)	1.80732	σ* (S1–C10)	0.11228	25.75	0.47	0.100
n1 (N3)	1.80732	π* (C17–C18)	0.37690	12.77	0.37	0.064
n2 (O5)	1.83777	π* (C22–C21)	0.38608	30.98	0.34	0.097
n1 (N2)	1.63308	π* (C9–O3)	0.28608	54.70	0.27	0.112
n1 (N2)	1.63308	π* (N3–C10)	0.27332	44.18	0.28	0.103
π* (C16–C15)	0.38405	π* (C14–C13)	0.33235	281.71	0.01	0.080
π* (O1–N1)	0.63210	π* (C1–C6)	0.38966	16.75	0.14	0.060
π* (C9–O3)	0.28608	π* (C7–C8)	0.21467	134.78	0.01	0.071
π* (N3–C10)	0.27332	π* (C17–C18)	0.02535	15.97	0.02	0.029

Table 5. NBO results showing formation of Lewis and non-Lewis orbital for the title compound.

Bond (AB)	ED/energy (a.u.)	EDA (%)	EDB (%)	NBO	S (%)	p (%)	d (%)
σ (C1–C6)	1.97633	51.03	48.97	0.7143 (sp$^{1.65}$) C+ 0.6998 (sp$^{1.98}$) C	37.68 / 33.50	62.29 / 66.46	0.03 / 0.05
π (C1–C6)	1.63134	54.53	45.47	0.7385 (sp$^{1.00}$) C+ 0.6743 (sp$^{1.00}$) C	0.00 / 0.00	99.99 / 99.95	0.01 / 0.05
σ*(C1–C6)	0.02229	48.97	51.03	0.6998 (sp$^{1.65}$) C-0.7143 (sp$^{1.98}$) C	37.68 / 33.50	62.29 / 66.46	0.03 / 0.05
π*(C1–C6)	0.38966	45.47	54.53	0.6743 (sp$^{1.00}$) C-0.7385 (sp$^{1.00}$) C	0.00 / 0.00	99.99 / 99.95	0.01 / 0.05
σ (C2–C3)	1.97569	50.19	49.81	0.7085 (sp$^{1.80}$) C+ 0.7057 (sp$^{1.83}$) C	35.65 / 35.38	64.31 / 64.58	0.04 / 0.04
π (C2–C3)	1.66209	48.65	51.35	0.6975 (sp$^{1.00}$) C+ 0.7166 (sp$^{1.00}$) C	0.00 / 0.00	99.95 / 99.96	0.05 / 0.04
σ*(C2–C3)	0.01419	49.81	50.19	0.7057 (sp$^{1.80}$) C-0.7085 (sp$^{1.83}$) C	35.65 / 35.38	64.31 / 64.58	0.04 / 0.04
π* (C2–C3)	0.27849	51.35	48.65	0.7166 (sp$^{1.00}$) C-0.6975 (sp$^{1.00}$) C	0.00 / 0.00	99.95 / 99.96	0.05 / 0.04
σ (C4–C5)	1.97565	51.22	48.78	0.7156 (sp$^{2.02}$) C+ 0.6985 (sp$^{1.88}$) C	33.13 / 34.76	66.83 / 65.20	0.04 / 0.04
π (C4–C5)	1.58603	49.92	50.08	0.7065 (sp$^{1.00}$) C+ 0.7077 (sp$^{1.00}$) C	0.00 / 0.00	99.97 / 99.96	0.03 / 0.04
σ*(C4–C5)	0.02090	48.78	51.22	0.6985 (sp$^{2.02}$) C-0.7156 (sp$^{1.88}$) C	33.13 / 34.76	66.83 / 65.20	0.04 / 0.04
π*(C4–C5)	0.37850	50.08	49.92	0.7077 (sp$^{1.00}$) C-0.7065 (sp$^{1.00}$) C	0.00 / 0.00	99.97 / 99.96	0.03 / 0.03
π (C7–C8)	1.84225	46.31	53.69	0.6805 (sp$^{1.00}$) C+ 0.7327 (sp$^{1.00}$) C	0.00 / 0.00	99.95 / 99.97	0.05 / 0.03
π* (C7–C8)	0.21467	53.69	46.31	0.7327 (sp$^{1.00}$) C-0.6805 (sp$^{1.00}$) C	0.00 / 0.00	99.95 / 99.97	0.05 / 0.03
π* (C9–O3)	0.28608	68.81	31.19	0.8295 (sp$^{1.00}$) C-0.5585 (sp$^{1.00}$) O	0.00 / 0.00	99.83 / 99.68	0.17 / 0.32
σ (C7–H7)	1.96338	63.53	36.47	0.7971 (sp$^{2.76}$) C+0.7358 (sp$^{4.80}$) H	26.60 / 17.14	73.30 / 82.21	0.10 / 0.65
σ* (C8–S1)	0.03789	45.86	54.14	0.6772 (sp$^{2.76}$) C-0.7358 (sp$^{4.80}$) S	26.60 / 17.14	73.30 / 82.21	0.10 / 0.65
π (O1–N1)	1.98523	60.13	39.87	0.7754 (sp$^{1.00}$) O+0.6314 (sp$^{1.00}$) N	0.00 / 0.00	99.75 / 99.73	0.25 / 0.27
σ* (C1–N1)	0.10337	62.18	37.82	0.7885 (sp$^{3.07}$) C-0.6150 (sp$^{1.76}$) N	24.55 / 36.28	75.31 / 63.69	0.14 / 0.03
σ* (O2–N1)	0.05677	48.62	51.38	0.6973 (sp$^{2.99}$) O-0.7168 (sp$^{2.14}$) N	25.05 / 31.80	74.81 / 68.10	0.14 / 0.10

Table 5 (*continued*)

Bond (AB)	ED/energy (a.u.)	EDA (%)	EDB (%)	NBO	S (%)	p (%)	d (%)
π^* (N3–C10)	0.27332	39.94	60.06	0.6320 (sp$^{99.99}$) N-0.775 (sp$^{99.99}$) C	0.38	99.38	0.24
					0.39	99.51	0.10
σ^* (C8–C9)	0.08180	47.58	52.42	0.6898 (sp$^{2.17}$) C-0.7240 (sp$^{1.83}$) C	31.53	68.42	0.05
					35.35	64.59	0.06
σ^* (C9–N2)	0.09450	64.11	35.89	0.8007 (sp$^{2.26}$) C-0.5991 (sp$^{2.04}$) N	30.62	69.25	0.12
					32.91	67.06	0.03
π^* (C16–C15)	0.38405	54.24	45.76	0.7365 (sp$^{1.00}$) C-0.6764 (sp$^{1.00}$) C	0.00	99.95	0.05
					0.00	99.96	0.04
σ^* (S1–C10)	0.11228	52.48	47.52	0.7244 (sp$^{5.60}$) S-0.6894 (sp$^{2.48}$) C	15.06	84.35	0.59
					28.68	71.22	0.10
π^* (C17–C18)	0.37690	48.88	51.12	0.6991 (sp$^{99.99}$) C-0.7150 (sp$^{99.99}$) C	0.03	99.93	0.04
					0.02	99.93	0.04
π^* (C22–C21)	0.38608	52.95	47.05	0.7277 (sp$^{1.00}$) C-0.6859 (sp$^{1.00}$) C	0.00	99.95	0.04
					0.00	99.96	0.04
π^* (C9–O3)	0.01086	64.88	35.12	0.8055 (sp$^{1.95}$) C-0.5926 (sp$^{1.38}$) C	33.87	66.03	0.09
					41.81	57.84	0.35
π^* (C14–C13)	0.33235	52.05	47.95	0.7214 (sp$^{1.00}$) C-0.6925 (sp$^{1.00}$) C	0.00	99.96	0.04
					0.00	99.96	0.04
n2(O2)	1.89839			(sp$^{99.99}$)	0.15	99.75	0.10
n3(O2)	1.44613			(sp$^{1.00}$)	0.00	99.78	0.22
n2 (O1)	1.89839			(sp$^{99.99}$)	0.15	99.75	0.10
n2 (S1)	1.76144			(sp$^{1.00}$)	0.00	99.91	0.08
n2 (O3)	1.84216			(sp$^{1.00}$)	0.00	99.75	0.25
n2 (O4)	1.83710			(sp$^{1.00}$)	0.00	99.91	0.09
n1 (N3)	1.80732			(sp$^{2.75}$)	26.59	73.24	0.17
n2 (O5)	1.83777			(sp$^{1.00}$)	0.00	99.90	0.09
n1 (N2)	1.63308			(sp$^{99.99}$)	0.20	99.79	0.01

reveal solvent contact with the $C_{24}H_{19}N_3O_5S$ molecule. Probing into ligplot interaction shows hydrogen bonding between H-atom of aromatic ring of $C_{24}H_{19}N_3O_5S$ molecule with O-atom of LeusineLeu(519) of acetylcholinesterase (Figure 12B). We can deduce that Leu (380), Phe (535), Ala (377) and Phe (531) developed hydrophobic interactions with $C_{24}H_{19}N_3O_5S$ molecule. On the other hand, Butyrylcholinesterase furnished only Vander Waal's interactions with $C_{24}H_{19}N_3O_5S$ molecule as indicated in ligplot of Butyrylcholinesterase (Figure 12D). Due to more considerable interactions acetylcholinesterase showed higher binding constant and greater spontaneity of reaction (more negative free energy values).

For the comprehensive understanding of macroscopic interaction, a number of electronic and steric descriptors have been calculated on the basis of molecular docking data (Table 6). Energies of frontier molecular orbitals i.e.; E_{HOMO} and E_{LUMO} are measure of electron donating and accepting character of a compound [50]. The compounds are considered to be strong electron as they are donating to who has more significant value of E_{HOMO}, and those compounds which have a low value of E_{LUMO}, have grander tendency to accept electrons. Therefore, in the present study $C_{24}H_{19}N_3O_5S$ molecule acts as electron donors while associating with Butylcholinesterase due immenser E_{HOMOc} as compared to its interaction with Actylcholinesterase due to smaller E_{HOMO}. This shows that when $C_{24}H_{19}N_3O_5S$ molecule networks with acetylcholinesterase, it withdraws electrons from enzyme residues thus developing strong interactions and high binding strength leading to greater value of binding constant (Table 7). Steric descriptor calculated from simulation results were molar refractivity (M_R), heat of formation (H_f) and hydrophobic surface volume (V_{surf}). M_R, which is a measure of the polarizability of the molecule and is directly related with the binding strength, was found to be higher for acetylcholinesterase furnishing the huger binding strength
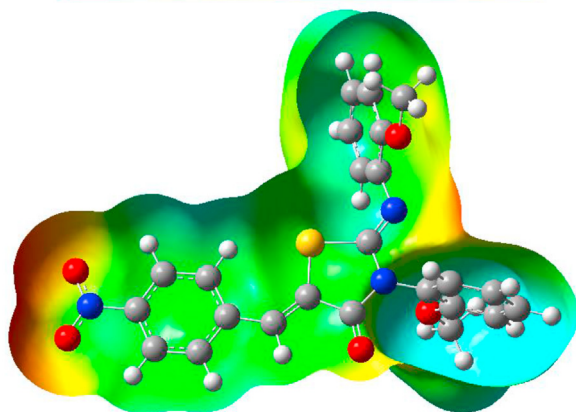

Figure 10. Molecular electrostatic potential (MEP) map calculated with B3LYP/6-31G(d, p) functional.
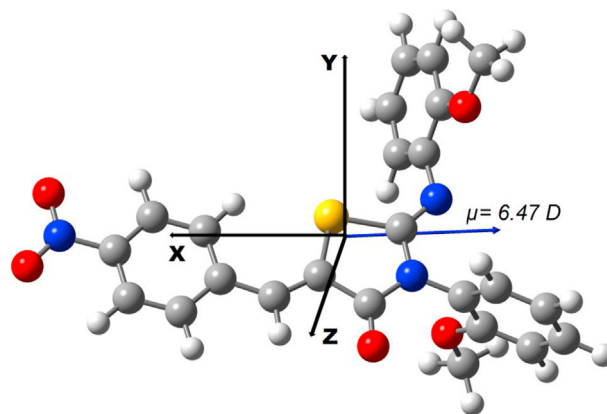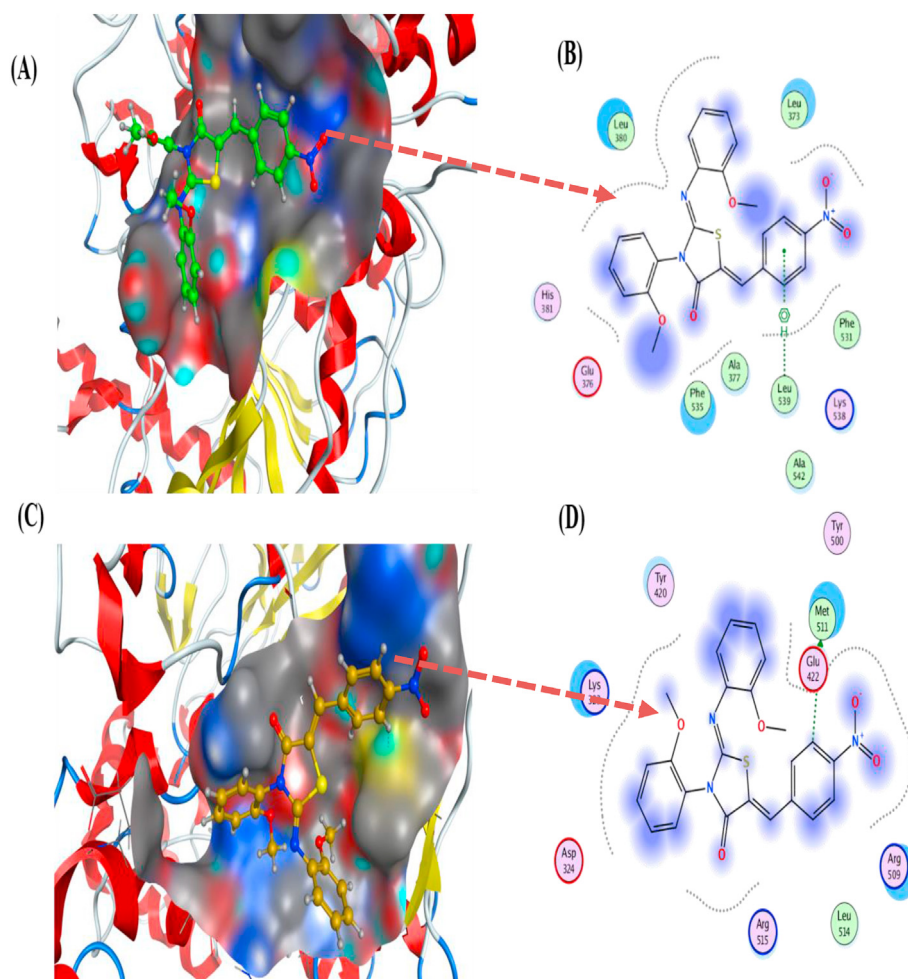

Figure 11. Orientation of the molecular dipole moment of the $C_{24}H_{19}N_3O_5S$ molecule; the origin is at the center of mass of the molecule.

Figure 12. Pose view analysis of molecular docked complexes of (A) Acetylcholinesterase, (C) Butyrylcholinesterase with $C_{24}H_{19}N_3O_5S$ molecules and their ligplots (B and D) calculated at PM3 semi-empirical level.

Table 6. Binding constants and free energy values of $C_{24}H_{19}N_3O_5S$ molecule for the Acetylcholinesterase and Butylcholinesyerase calculated from molecular docking data.

Complex code	Molecular docking	
	"K_b"/M^{-1}	(-ΔG) KJmol^{-1}
Acet –2	1.70×10^4	-24.14
Buty–2	1.06×10^3	-17.25

Table 7. Data set of electronic descriptors calculated from molecular docking data.

Complexes	E_{HOMO} (kcal/mol)	E_{LUMO} (kcal/mol)	E_{ele} (kcal/mol)	E_{vander} (kcal/mol)	E_{IP} (kcal/mol)	E_{Total} (kcal/mol)
Acet-2	-9.18822	-1.7942	-1034645.0	12.6166945	9.1882	-122140.09
Buty-2	-8.92967	-1.537209	-1043527.7	15.312981	-8.929670	-121562.9

Table 8. Data set of steric descriptors calculated from Molecular docking data.

Complexes	H_f (kcal/mol)	M_R	Slog P	V_{surf}	Dipole
Acet-2	16.12	12.1500	5.0136	458.18	4.3368
Buty-2	16.86	11.5960	5.426	447. 78	8.3612

of Acetylcholinesterase with $C_{24}H_{19}N_3O_5S$ molecule, Table 8, stable and strong complexes have smaller positive value of heat of formation (H_f). In this work, Acetylcholinesterase has smaller positive value of heat of formation (H_f) with stronger complex formation and high binding constant as compared to Butyrylcholinesterase (Table 8). It was also observed that the value of hydrophobic surface volume (V_{surf}) is comparatively bigger for Actylcholinesterase than Butyrylcholinesterase due to the greater hydrophobic surface contact of the compound PB with Acetylcholinesterase. Higher hydrophobic surface area is attributed to the huger overlapping of $C_{24}H_{19}N_3O_5S$ molecule with a greater number of enzyme residues.

5. Conclusion

The molecular system(2Z.5Z)-5-(4-nitrobenzylidene)-3-N(2 methoxyphenyl)-2-N′(2-methoxyphenylimino) thiazolidin-4-one, has been synthesized and characterized by FT-IR, UV(^{1}H,^{13}C) NMR spectroscopy and single crystal X-ray diffraction techniques. We investigated the optimized molecular structure and related harmonic vibrational frequencies, UV-visible,^{1}H and ^{13}C NMR chemical shifts using density functional theory with the hybrid functional B3LYP in combination with 6-31G(d, p) basis set. DFT calculations and comparison of proton and carbon NMR chemical shifts have been a supplementary tool for confirming the correctness of the structure. The comprehensive vibrational analysis of the molecule has shown an excellent concordance with secured experimental data. However, differences observed between the experimental and computed values are associated to the assumption of considering the simulated compound as a single molecule in the gas phase, whereas the experimental values were recorded in the solid phase by exploring the presence of intermolecular interactions. Furthermore, the UV-Vis spectrum was obtained in chloroform solution. The stability of the molecule arising from hyper-conjugated interaction and charge delocalization has been explored with NBO tool. Also, we have reported HOMO and LUMO energies and energy band gap with the hybrid B3LYP method. The slight difference in energy band gap between HOMO and LUMO has shown that synthesized molecule carries high charge mobility with small excitation energy. These results made $C_{24}H_{19}N_3O_5S$ molecule potentially easy to polarize. Molecular electrostatic potential indicates clearly that the oxygen and nitrogen atoms are the most reactive sites in the electrophilic attack, while the preferred sites for the nucleophilic attack are on the phenyl and methyl groups. We completed the present investigations with molecular docking in order to understand the covalent and non-covalent interactions between the present $C_{24}H_{19}N_3O_5S$ molecule and enzymes: Acetyl cholinesterase and Butyrylcholinesterase. We hope that the synthesis, crystallographic and spectroscopic characterization and DFT studies of (2Z.5Z)-5-(4-nitrobenzylidene)-3-N(2-methoxyphenyl)-2-N'(2-methoxyphenylimino) thiazolidin-4-one will be useful in designing new devices for organic electronics based biological materials.

Declarations

Author contribution statement

Ahmed Djafri, Fouzia Perveen, Rachida Rahmani, Souraya Goumri-Said: Conceived and designed the experiments; Performed the experiments; Analyzed and interpreted the data; Contributed reagents, materials, analysis tools or data; Wrote the paper.

Nadia Benhalima, Nawel Khelloul, Rachida Rahmani, Ayada Djafri, Abdelkader Chouaih, Mohammed Benali Kanoun: Conceived and designed the experiments; Analyzed and interpreted the data; Contributed reagents, materials, analysis tools or data; Wrote the paper.

Data availability statement

Data will be made available on request.

Declaration of interests statement

The authors declare no conflict of interest.

Additional information

No additional information is available for this paper.

References

[1] J.C. Cuevas, E. Scheer, Molecular Electronics: an Introduction to Theory and Experiment, World Scientific, Singapore, 2010.

[2] C.M. Niemeyer, C.A. Mirkin (Eds.), Nanobiotechnology: Concepts, Applications and Perspectives, Wiley-VCH, Weinheim, Germany, 2004.

[3] N.S. Sariciftci, L. Smilowitz, A.J. Heeger, F. Wudl, Photoinduced electron transfer from a conducting polymer to Buckminsterfullerene, Science 258 (1992) 1474–1476.

[4] S.S. Sun, N.S. Sariciftci (Eds.), Organic Photovoltaics: Mechanisms, Materials, and Devices, CRC Press, 2005.

[5] M.L. Perrin, E. Burzurí, H.S.J. van der Zant, Single-molecule transistors, Chem. Soc. Rev. 44 (2015) 902–919.

[6] A. Aviram, M.A. Ratner, Molecular rectifiers, Chem. Phys. Lett. 29 (1974) 277–283.

[7] H. Chen, J. Bai, L. Jiao, Z. Guo, Q. Yin, X. Li, Design, microwave-assisted synthesis and HIV-RT inhibitory activity of 2-(2,6-dihalophenyl)-3-(4,6-dimethyl-5-(un) substituted-pyrimidin-2-yl)- thiazolidin-4-ones, Bioorg. Med. Chem. 17 (2009) 3980–3986.

[8] G. Küçükgüzel, A. Kocatepe, E. De Clercq, F. Şahin, M. Güllüce, Synthesis and biological activity of 4-thiazolidinones, thiosemicarbazides derived from diflunisalhydrazide, Eur. J. Med. Chem. 41 (2006) 353–359.

[9] K. Appalanaidu, R. Kotcherlakota, T.L. Dadmal, V.S. Bollu, R.M. Kumbhare, C.R. Patra, Synthesis and biological evaluation of novel 2-imino-4- thiazolidinone derivatives as potent anti-cancer agents, Bioorg. Med. Chem. Lett 26 (2016) 5361–5368.

[10] C.B. Mishra, S. Kumari, M. Tiwari, Thiazole: a promising heterocycle for the development of potent CNS active agents, Eur. J. Med. Chem. 92 (2015) 1–34.

[11] A. Aldo, M. Granaiola, A. Leoni, A. Locatelli, R. Morigi, R. Rambaldi, Synthesis and antitubercular activity of imidazo[2,1-b] thiazoles, Eur. J. Med. Chem. 36 (2001) 743–746.

[12] J. Clough, S. Chen, E.M. Gordon, C. Hackbarth, S. Lam, J. Trias, J. Richard, G. Candiani, S. Donadio, G. Romano, R. Ciabatti, J.W. Jacobs, Combinatorial modification of natural products: synthesis and in vitro analysis of derivatives of thiazole peptide antibiotic GE2270 A: a-ring modifications, Bioorg. Med. Chem. Lett 13 (2003) 3409–3414.

[13] N.D. Gaikwad, S.V. Patil, V.D. Bobade, Synthesis and biological evaluation of some novel thiazole substituted benzotriazole derivatives, Bioorg. Med. Chem. Lett 22 (2012) 3449–3454.

[14] A. Beauchard, A. Jaunet, L. Murillo, B. Baldeyrou, A. Lansiaux, J. Cherouvrier, L. Domon, L. Picot, C. Bailly, T. Besson, V. Thiery, Synthesis and antitumoral activity of novel thiazolobenzotriazole, thiazoloindolo[3,2-c]quinoline and quinolinoquinoline derivatives, Eur. J. Med. Chem. 44 (2009) 3858–3865.

[15] A. Djafri, A. Chouaih, J.C. Daran, A. Djafri, F. Hamzaoui, Crystal and molecular structure of (2Z,5Z)-3-(2-methoxyphenyl)-2-[(2-methoxyphenyl) imino] -5-(4-nitro benzylidene) thiazolidin-4-one, ActaCryst E73 (2017) 511–514.

[16] M. Mohamad, R. Ahmed, A. Shaari, S. Goumri-Said, Structure-dependent optoelectronic properties of perylene, di-indenoperylene (DIP) isolated molecule and DIP molecular crystal, Chem. Cent. J. 11 (1) (2017) 125.

[17] R. Martin, Electronic Structure: Basic Theory and Practical Methods, Cambridge University Press, 2008.

[18] D. Jacquemin, J. Preat, M. Charlot, V. Wathelet, J.M. Andre, E.A. Perpete, Theoretical investigation of substituted anthraquinone dyes, Chem. Phys. 121 (2004) 1736–1743.

[19] E.H. Anouar, J.F.F. Weber, Time-dependent density functional theory study of UV/vis spectra of natural styrylpyrones, Spectrochim. Acta A 115 (2013) 675–682.

[20] K. Wolinski, J.F. Hinton, P. Pulay, Efficient implementation of the gauge-independent atomic orbital method for NMR chemical shift calculations, J. Am. Chem. Soc. 112 (1990) 8251–8260.

[21] E.H. Anouar, S.A.A. Shah, N.B. Hassan, N.E. Moussaoui, R. Ahmad, M. Zulkefeli, J.F.F. Weber, Antioxidant activity of hispidin oligomers from medicinal fungi: a DFT study, Molecules 19 (2014) 3489–3507.

[22] M.J. Frisch, G.W. Trucks, H.B. Schlegel, G.E. Scuseria, M.A. Robb, J.R. Cheeseman, J.A. Montgomery Jr., T. Vreven, K.N. Kudin, J.C. Burant, J.M. Millam, S.S. Iyengar, J. Tomasi, V. Barone, B. Mennucci, M. Cossi, G. Scalmani, N. Rega, G.A. Petersson, H. Nakatsuji, M. Hada, M. Ehara, K. Toyota, R. Fukuda, J. Hasegawa, M. Ishida, T. Nakajima, Y. Honda, O. Kitao, H. Nakai, M. Klene, X. Li, J.E. Knox, H.P. Hratchian, J.B. Cross, V. Bakken, C. Adamo, J. Jaramillo, R. Gomperts, R.E. Stratmann, O. Yazyev, A.J. Austin, R. Cammi, C. Pomelli, J.W. Ochterski, P.Y. Ayala, K. Morokuma, G.A. Voth, P. Salvador, J.J. Dannenberg, V.G. Zakrzewski, S. Dapprich, A.D. Daniels, M.C. Strain, O. Farkas, D.K. Malick, A.D. Rabuck, K. Raghavachari, J.B. Foresman, J.V. Ortiz, Q. Cui, A.G. Baboul, S. Clifford, J. Cioslowski, B.B. Stefanov, G. Liu, A. Liashenko, P. Piskorz, I. Komaromi, R.L. Martin, D.J. Fox, T. Keith, M.A. Al-Laham, C.Y. Peng, A. Nanayakkara, M. Challacombe, P.M.W. Gill, B. Johnson, W. Chen, M.W. Wong, C. Gonzalez, J.A. Pople, Gaussian 03, Revision C.02, Gaussian, Inc., Wallingford CT, USA, 2004.

[23] A.E. Frisch, A.B. Nielsen, A.J. Holder, Gaussview, Gaussian Inc., Pittsburg, USA, 2003.

[24] A.D. Becke, Density-functional thermochemistry. V. Systematic optimization of exchange-correlation functional, J. Chem. Phys. 107 (1997) 8554–8560.

[25] G. Rauhut, P. Pulay, Transferable scaling factors for density functional derived vibrational force fields, J. Phys. Chem. 99 (1995) 3093–3100.

[26] R. Fletcher, M.J.D. Powell, A rapidly convergent descent method for minimization, Comput. J. 6 (1963) 163–168.

[27] R.F. Bader, Atoms in Molecules. A Quantum Theory, Clarendon Press, Oxford, GB, 1990.

[28] M.A. Spackman, D. Jayatilaka, Hirshfeld surface analysis, CrystEngComm 11 (1) (2009) 19–32.

[29] S.K. Wolff, D.J. Grimwood, J.J. Mckinnon, D. Jayatilaka, M.A. Spackmann, Crystal Explorer 3.0, University of Western Australia, Perth, Western Australia, 2007.

[30] M.H. Jamroz, Vibrational Energy Distribution Analysis, VEDA 4 Computer Program, Poland, 2004.

[31] National Institute of Standards and Technology, Vibrational frequency scaling factor as determined from data in the CCCBDB. https://cccbdb.nist.gov/vibscalejustx.asp.

[32] J.B. Lambert, H.F. Shurvell, L. Verbit, R.G. Cooks, G.H. Stout, Organic Structural Analysis, Macmillan Publ. Co. Inc., New York, 1976.

[33] A. Fu, D. Du, Z. Zhou, Density functional theory study of vibrational spectra of acridine and phenazine, Spectrochim. Acta Mol. Biomol. Spectrosc. 59 (2003) 245–253.

[34] M. Boulakoud, K. Toubal, S. Yahiaoui, A. Chouaih, G. Chita, A. Djafri, F. Hamzaoui, Molecular structure investigation of Z-3N(2-ethoxyphenyl)-2-N'(2-ethoxy phenyl)-imino-thiazolidin-4-one by ab initio, DFT and X-ray diffraction methods, J. Struct. Chem. 56 (2015) 1373–1378.

[35] C.S. Chidan Kumar, K. Govindarasu, H.K. Fun, E. Kavitha, S. Chandraju, C.K. Quah, Synthesis, molecular structure, spectroscopic characterization and quantum

[36] chemical calculation studies of (2E)-1-(5-chlorothiophen-2-yl)-3-(2,3,4-trimethoxy phenyl) prop-2-en-1-one, J. Mol. Struct. 1085 (2015) 63–77.

[36] N.P.G. Roeges, A Guide to the Complete Interpretation of the Infrared Spectra of Organic Structures, Wiley, New York, 1994.

[37] B. Smith, Infrared Spectral Interpretation, A Systematic Approach, CRC Press, Washington, DC, 1999.

[38] M. Mamaghani, A. Loghmanifar, M.R. Taati, An efficient one-pot synthesis of new 2-imino-1,3-thiazolidin-4-ones under ultrasonic conditions, Ultrason. Sonochem. 18 (2011) 45–48.

[39] Y. Megrouss, F.T. Baara, N. Boukabcha, A. Chouaih, A. Hatzidimitriou, A. Djafri, F. Hamzaoui, Synthesis, X-ray structure determination and related physical properties of thiazolidinone derivative by DFT quantum chemical method, Acta Chim. Slov. 66 (2019) 1–11.

[40] B. Kosar, C. Albayrak, Spectroscopic investigations and quantum chemical computational study of (E)-4-methoxy-2-[(p-tolylimino)methyl]phenol, Spectrochim. Acta Mol. Biomol. Spectrosc. 78 (2010) 160–167.

[41] B.J. Powell, T. Baruah, N. Bernstein, K. Brake, R.H. McKenzie, P. Meredith, M.R. Pederson, A first-principles density-functional calculation of the electronic and vibrational structure of the key melanin monomers, J. Chem. Phys. 120 (2004) 8608–8615.

[42] N.H. Belkafouf, F.T. Baara, A. Altomare, R. Rizzi, A. Chouaih, A. Djafri, F. Hamzaoui, Synthesis, PXRD structural determination, Hirshfeld surface analysis and DFT/TD-DFT investigation of 3N-ethyl-2N`-(2-ethylphenylimino) thiazolidin-4-one, J. Mol. Struct. 1189 (2019) 8–20.

[43] J.C.S. Costa, R.J.S. Taveira, C.F.R.A.C. Lima, A. Mendes, L.M.N.B.F. Santos, Optical band gaps of organic semiconductor materials, Opt. Mater. 58 (2016) 51–60.

[44] E.D. Glendening, A.E. Reed, J.E. Carpenter, F. Weinhold, NBO 3.1, theoretical ChemestryInstituten, University of Wisconsin, Madison, WI, 1998.

[45] R. Rahmani, N. Boukabcha, A. Chouaih, F. Hamzaoui, S. Goumri-Said, On the molecular structure, vibrational spectra, HOMO-LUMO, molecular electrostatic potential, UV-Vis, first order hyperpolarizability, and thermodynamic investigations of 3-(4-chlorophenyl)-1-(1yridine-3-yl) prop- 2-en-1-one by quantum chemistry calculations, J. Mol. Struct. 1155 (2018) 484–495.

[46] M. Drissi, N. Benhalima, Y. Megrouss, R. Rahmani, A. Chouaih, F. Hamzaoui, Theoretical and experimental electrostatic potential around the m-nitrophenol molecule, Molecules 20 (2015) 4042–4045.

[47] N. Boukabcha, A. Djafri, Y. Megrouss, Ö. Tamer, D. Avcı, N. Dege, A. Chouaih, Y. Atalay, A. Djafri, F. Hamzaoui, Synthesis, crystal strucure , spectroscopic characterization and nonlinear optical properties of (Z)-N'-(2,4-dinitrobenzylidene)-2-(quinolin-8-yloxy) acetohydrazide, J. Mol. Structr. 1194 (2019) 112–123.

[48] https://pubmed.ncbi.nlm.nih.gov/20408548/, 2010.

[49] https://pubmed.ncbi.nlm.nih.gov/15667209/, 2005.

[50] Perveen Fouzia, et al., Electrochemical, spectroscopic and theoretical monitoring of anthracyclines' interactions with DNA and ascorbic acid by adopting two routes: cancer cell line, studies, PLoS One 13 (10) (2018), e0205764.

[51] T. Akram, M.A. Abbasi, A. Mahmood, E. Barboza de Lima, F. Perveen, M. Ashraf, I. Ahmad, S. Goumri-Said, Synthesis, molecular structure, spectroscopic properties and biological evaluation of 4-substituted-N-(1H-tetrazol-5-yl)benzenesulfona-mides: combined experimental, DFT and docking study, J. Mol. Struct. 1195 (2019) 119–130.